photonics

MDPI

Article

Optical Design for Aberration Correction of Ultra-Wide Spectral Range Echelle Spectrometer

Yuming Wang [1,2], Youshan Qu [1], Hui Zhao [1] and Xuewu Fan [1,*]

[1] Space Optical Technology Research Department, Xi'an Institute of Optics and Precision Mechanics, Chinese Academy of Sciences, 17 Xinxi Road, Xi'an 710119, China
[2] School of Optoelectronics, University of Chinese Academy of Sciences, Beijing 100049, China
* Correspondence: fanxuewu@opt.ac.cn

Abstract: The echelle grating spectrometer, with a wide spectral range and high-resolution spectral analysis, is one of the best tools for fine spectral measurement. Nevertheless, it suffers from excessive residual aberrations and a large overall size. In this study, the design and implementation of a novel asymmetric Czerny–Turner ultra-wide spectral range achromatic echelle spectrometer are described. The echelle spectrometer has three channels, and it uses an off-axis parabolic mirror to obtain collimated light without aberrations. Three sets of gratings and dispersive prisms with different coatings are utilized as cross-dispersion elements to acquire two-dimensional images containing spectral information. Suitable detectors are selected according to the requirements of each channel, and three sets of coaxial focusing lenses are designed separately to minimize the aberration. The results of the simulation analysis by ZEMAX indicate that in the entire operating band (200–1100 nm), the root mean square radius of the dispersion spots is ≤ 2.2 μm, all of which are located within the limited range of the size of the detector, thus ensuring that the system's spectral resolution reaches 0.02 nm at 200 nm, 0.04 nm at 650 nm, and 0.1 nm at 1100 nm.

Keywords: echelle spectrometer; ultra-wide spectral range; aberration correction; optical design

Citation: Wang, Y.; Qu, Y.; Zhao, H.; Fan, X. Optical Design for Aberration Correction of Ultra-Wide Spectral Range Echelle Spectrometer. *Photonics* **2022**, *9*, 841. https://doi.org/10.3390/photonics9110841

Received: 14 October 2022
Accepted: 5 November 2022
Published: 8 November 2022

Publisher's Note: MDPI stays neutral with regard to jurisdictional claims in published maps and institutional affiliations.



Copyright: © 2022 by the authors. Licensee MDPI, Basel, Switzerland. This article is an open access article distributed under the terms and conditions of the Creative Commons Attribution (CC BY) license (https://creativecommons.org/licenses/by/4.0/).

1. Introduction

The method of identifying substances and determining their chemical composition and relative content according to a spectrum is called spectral analysis. It is widely used in fields such as astronomy, national defense, agriculture, and medicine [1–3]. Therefore, the manufacture of high-resolution, wide spectral range, compact, and speedy-response spectroscopic instruments is of immense significance for the promotion of the development of science and technology.

In 1949, Harrison analyzed the characteristics, design, and manufacturing methods of echelle gratings and described the common design problems associated with the echelle spectrometer [4]. The echelle spectrometer uses an echelle grating as the main dispersion element and is equipped with auxiliary dispersion elements such as prisms or gratings, enabling the simultaneous direct acquisition of high-resolution, broadband spectral information without scanning. Given these advantages, the echelle spectrometer is one of the most effective tools for exploring the cosmos [5–9]. However, owing to the significant limitations of the manufacturing capability of the area array detector elements (particularly the near-infrared InGaAs detector) and the residual aberrations at the edge wavelength [10,11], the conventional symmetric Czerny–Turner (C–T) echelle spectrometer has difficulty meeting broad spectrum, high resolution, and high imaging quality requirements simultaneously [12,13]. Aberrations therefore need to be minimized to achieve the optimum performance of the individual components.

The main aberrations, common correction methods, and the advantages and disadvantages of the ordinary C–T spectrometer system structure are as follows:

(1) Spherical aberration: the field of view of the echelle spectrometer is generally small, and the influence of spherical aberrations can be reduced through optical design. There are two common solutions: first, according to the Rayleigh criterion, if the system F-number is defined as $F^{\#} = f' / D$ and the relationship between the system focal length f' and the F-number $F^{\#}$ satisfies $f' \leq 256\lambda(F^{\#})^4$, the spherical aberration has little influence [14]; second is the use of off-axis parabolic mirrors, which can focus collimated light without introducing spherical aberrations [15] at the expense of a worse coma for off-axis beams.
(2) Coma: the most common method for eliminating coma in C–T spectrometers is the combination of collimating and focusing mirrors with the same curvature radius and opposite off-axis angles proposed by inventors Czerny and Turner. Later, the asymmetric structure was developed, which can also eliminate the coma of a specific wavelength when certain conditions are met [16]. However, these methods are limited to a single wavelength and the problem can only be partially offset in the rest of the wavelength range by the collimating and focusing mirrors with the opposite sign of the coma.
(3) Astigmatism: to eliminate the astigmatism of the C–T grating spectrometer, it is necessary to add additional elements such as a lens [17], e.g., an aspherical or free-form cylindrical lens [18], and toroidal mirrors [19]. In addition, Wood and Lawler devised a method of rotating auxiliary dispersive elements [20]. However, the aforementioned methods impose high demands on optical processing and assembly, resulting in high costs and long cycles, which are not conducive to product industrialization.

In addition, the collimating and focusing mirrors of the conventional C–T spectrometer have the same curvature radius; thus, the optical system magnification ratio is 1:1. In other words, without considering the aberration, the size of the ideal slit spectral image corresponding to each wavelength on the detector is the same as the slit size. To achieve the best match between the spectral resolution and detector performance, the pixel size (after binning) must be equal to or slightly smaller than the slit size.

Furthermore, the spectral resolution is also limited by the number of pixels, especially in the near-infrared (NIR) spectral range. The number of pixels in a conventional InGaAs NIR area array detector is 640 × 512. There is clearly a trade-off between a wide spectral range and high spectral resolution.

In previous studies, the use of a spherical or parabolic reflector for focusing has been a common approach, and this has the advantages of a simple structure and no chromatic aberrations. However, with the increasing demand for ultraviolet (UV) to NIR broadband applications for atomic, molecular, and fluorescence spectroscopy, there are additional problems that need to be addressed for system optimization. First, the residual aberrations at the edge wavelengths of each order are particularly significant compared with those at the center wavelengths due to the lower aberration correction capability of individual mirrors. Second, the characteristics of high spectral resolution, wide wavelength range, and compact structure are difficult to satisfy simultaneously due to the detector performance and size. In this study, the core indicators of the echelle spectrometer and its main influencing factors are analyzed, and a new type of asymmetric C–T ultra-wide spectrum achromatic high-resolution echelle spectrometer that uses an off-axis parabolic mirror for collimating and three sets of coaxial lens for focusing is proposed. The spectrometer minimizes aberrations, increases system robustness, reduces the requirements for detectors, and reduces the difficulty and cycle of processing and assembly while ensuring high resolution across a wide spectral range. The spectrometer operates at a wavelength of 200–1100 nm, and the size of the ideal slit spectral image corresponding to each wavelength on the detector is slightly smaller than the pixel size of the detector (after binning). Moreover, the root mean square (RMS) radius of the dispersion spots over the entire spectral range is ≤ 2.2 μm. As a result, the aberrations have been corrected effectively, ensuring that the spectral resolution of the spectrometer reaches 0.02 nm at 200 nm, 0.04 nm at 650 nm, and 0.1 nm at 1100 nm.

2. Optical Layout of the Echelle Spectrometer

To realize the precise detection of multi-element spectral lines, the echelle grating spectrometer must meet the requirements of both a wide spectral range and high resolution. The specific design parameters are shown in Table 1.

Table 1. Parameters of the designed system.

Parameter	Values
Detection spectrum	200–1100 nm
Spectral resolution	<0.1 nm (entire spectrum)
Slit size	25 × 25 μm
Collimator focal length	200 mm
Collimator aperture	25 mm

Since the detection spectra of the instrument span from deep UV to NIR, and considering the limitations of component manufacturing capability, the coating process, and synchronous response capability, the optical path is designed with three channels. The optical train designed by ZEMAX is depicted in Figure 1. The spectrometer adopts an asymmetric C–T structure with a compact layout and consists of six main components: a slit plane, a parabolic collimator, three echelle gratings, three dispersive prisms, three camera optics, and three detector arrays. Channels 1, 2, and 3 all use coaxial optical systems. It is worth noting that channel 1 uses a Cassegrain system for focusing because there are few types of UV glass, and most of them are expensive.

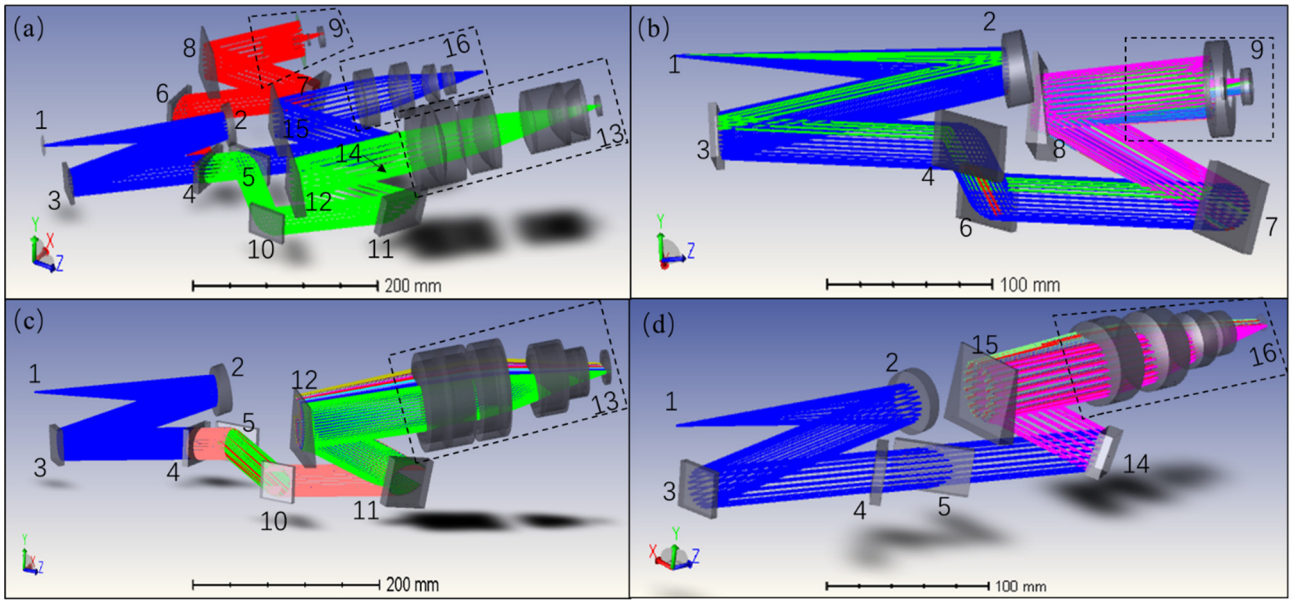


Figure 1. Optical path through the designed spectrometer. (**a**) Overall optical path of the spectrometer, (**b**) UV channel (channel 1), (**c**) visible channel (channel 2), and (**d**) NIR channel (channel 3). 1: slit; 2: off-axis parabolic collimating mirror; 3, 6, and 10: folding mirror; 4 and 5: beam splitter; 7, 11, and 14: echelle grating; 8, 12, and 15: dispersive prism; 9, 13, and 16: camera.

3. Theory and Design Method

3.1. Collimating Mirror

The off-axis parabolic mirror allows perfect imaging of the on-axis field of view conjugated at a finite distance, and there are no monochromatic or chromatic aberrations. Nonetheless, the off-axis field of view suffers from significant coma aberrations.

Although the echelle spectrometer designed in our study features a small field of view, the off-axis parabolic mirror is highly sophisticated in terms of its processing and detection technology, and it can be constructed quickly and at low cost. Therefore, an off-axis parabolic mirror is used for collimation. To reduce the size of the optical machine, the focal length of the off-axis parabolic mirror is set to 200 mm, and the effective clear aperture is 25 mm.

3.2. Detector

The main parameters of the detector are the spectral response characteristics, the number of saturated electrons, the quantum efficiency, the pixel size, and the number of pixels.

The spectral response characteristics are generally selected depending on the task requirements. The detector performance improves with an increasing number of saturated electrons and higher quantum efficiency. To achieve the same performance index, the smaller the pixel size p, the shorter the focal length of the corresponding optical system, which can further reduce the size, weight, and cost of the entire instrument. However, the reduction in the pixel size decreases the sensitivity of the detector. In addition, it increases the Nyquist spatial frequency, causing a reduction in the modulation transfer function of the optical system. In particular, as the pixel size approaches the diffraction limit, the design, processing, and assembly become considerably more difficult. To ensure the imaging quality, the F-number must be reduced, which inevitably increases the size and weight of the instrument. Therefore, all of these characteristics must be considered in the selection of the detector pixel size to achieve the best performance.

Suitable spectral resolution can be ensured on the basis of a sufficient number of pixels. For echelle spectrometers, the collection of the spectrum by the detector should comply with the Nyquist sampling theorem, i.e., the spatial distribution frequency of pixels must be twice the frequency of the variation in spectral profile. In other words, if the spectral resolution is r, the minimum center-to-center distance of the spots on the detector for adjacent spectra must satisfy $\Delta_{min} \geq 2p$. Furthermore, it was found that the lower the order of the echelle grating, the larger the free spectral range. If the longest free spectral region corresponding to the lowest working level is $\Delta\lambda_{max}$, to meet the resolution requirement, the number of pixels on the long side of the detector (after binning) must satisfy the following:

$$H_{pixel} \geq 2 \times \frac{\Delta\lambda_{max}}{r}. \quad (1)$$

According to the calculation result of Equation (1), a GSENSE5130 detector with a pixel size of 4.25 μm × 4.25 μm and a pixel number of 5056 × 2968 was set for channels 1 and 2. A GD6883-64015-MD NIR detector with a pixel size of 15 μm × 15 μm and a pixel number of 640 × 512 was set for channel 3. In this study, the pixels of the GSENSE5130 are merged (5 × 5 binning) to improve the performance of the instrument and ensure the feasibility of its optical design, processing, and adjustment while maintaining the spectral resolution. After merging, the pixel size of channels 1 and 2 is 21.25 μm × 21.25 μm, and the number of pixels is 1011 × 593.

3.3. Echelle Grating

The echelle spectrometer generally utilizes a non-cross C–T structure, and the echelle functions under the conditions of a quasi-Littrow configuration with an off-axis angle from the incident light [21].

3.3.1. Principles of Design or Selection

When the echelle grating satisfies the quasi-Littrow condition, for a certain order m, the diffraction follows the following equation:

$$m\lambda = dsin\beta_0 cos\gamma + dsin\beta' cos\gamma, \quad (2)$$

where d is the groove spacing of the echelle grating, β_0 is the blaze angle, β' is the diffraction angle, and γ is the off-axis angle. In particular, for the central wavelength λ_{cen},

$$m\lambda_{cen} = d\sin\beta_0\cos\gamma + d\sin\beta'\cos\gamma = 2d\sin\beta_0\cos\gamma. \quad (3)$$

The corresponding free spectral region $\Delta\lambda$ of this order is defined as the interval where the adjacent order spectra almost overlap. This can be written as follows:

$$m(\lambda + \Delta\lambda) = (m + 1)\lambda. \quad (4)$$

Equation (4) can be simplified as:

$$\Delta\lambda = \frac{\lambda_{cen}}{m}. \quad (5)$$

The angular dispersion of the echelle grating can be calculated using differentiating Equation (2):

$$\frac{d\beta}{d\lambda} = \frac{m}{d\cos\beta_0\cos\gamma}. \quad (6)$$

For a specific echelle grating, the wavelength, diffraction angle, free spectral region width, and dispersion ratios corresponding to each order of the echelle grating can be calculated according to Equations (2), (3), (5) and (6). For the same echelle grating, $dcos\beta_0$ is a constant. Therefore, when the wavelength is shorter, the working order is higher, the free spectral region is shorter, and the diffraction angle range is smaller. However, the angular dispersion is larger. Therefore, provided that the longest wavelength meets the spectral resolution requirements, a higher spectral resolution can be achieved in the short-wave direction.

3.3.2. Matching of Echelle Gratings and Detectors

Assuming that the maximum number of effective pixels in a single row (or single column) of the detector is H_{max}, regardless of the inclination and nonlinearity of the stripes, the largest free spectral region corresponding to the lowest order covering a single row (column) is used for calculation. According to Equation (1), the largest free spectral region should satisfy the following:

$$\Delta\lambda_{max} \leq \frac{H_{max} \times r}{2}. \quad (7)$$

According to Equation (6), the minimum order of the echelle grating can be calculated from the upper limit of the detection wavelength: $m_{min} \geq \left\lceil \frac{\lambda_{max}}{\Delta\lambda_{max}} \right\rceil$, where $\lceil\ \rceil$ means round up. Combined with Equation (4), the grating constant and the blaze angle must satisfy $d\sin\beta_0 \geq \frac{m_{min}\lambda_{cen-max}}{2\cos\gamma}$ to ensure the realization of full spectral resolution.

3.3.3. Comparison of Dispersion Capability of Different Echelle Gratings

Based on the parameters of the three different echelle gratings mentioned above, Figure 2 demonstrates the relationship between the diffraction angle and the angular dispersion corresponding to each wavelength under different working orders.

The variation ranges of the echelle angular dispersion of channels 1, 2, and 3 are 4.1426–10.3566, 5.2010–8.9672, and 2.5857–3.5461 mrad/nm, and the maximum diffraction angles are 2.2826°, 8.9313°, and 4.6398°, respectively. Among these, the echelle grating in channel 3 features a low working level and angular dispersion owing to the limited number of pixels.

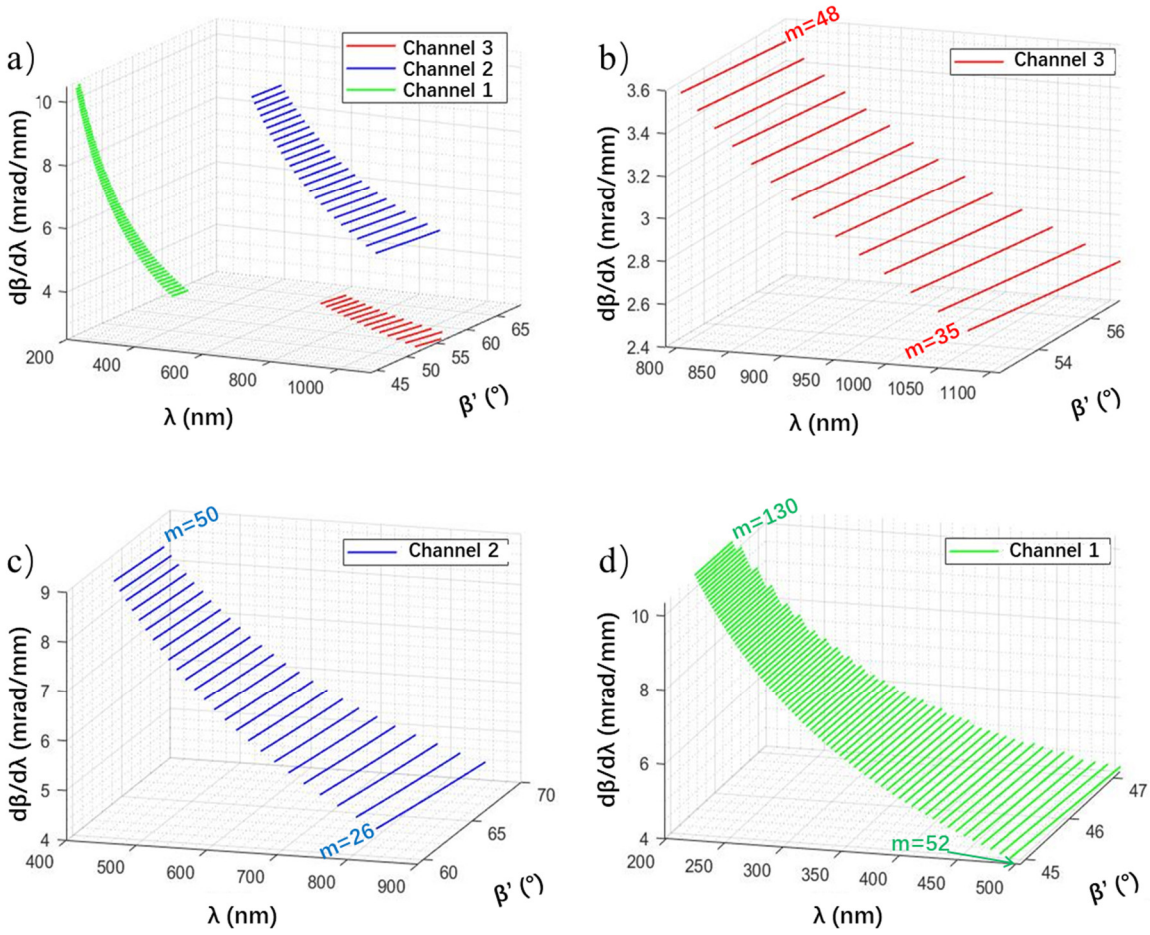


Figure 2. Wavelength–diffraction angle–angular dispersion relationship of the echelle gratings. (**a**) Schematic of the three channels, (**b**) channel 3, (**c**) channel 2, and (**d**) channel 1. $d\beta/d\lambda$ is the angular dispersion, β' is the diffraction angle, m is the order.

3.4. Dispersive Prism

The dispersion ability of a prism is evaluated based on the change in the refractive index in the medium at different wavelengths. The law of refractive index change with changing wavelength is most commonly expressed by the Sellmeier formula [22]:

$$n_\lambda^2 = 1 + \frac{K_1\lambda^2}{\lambda^2 - L_1} + \frac{K_2\lambda^2}{\lambda^2 - L_2} + \frac{K_3\lambda^2}{\lambda^2 - L_3}, \quad (8)$$

where K_i and L_i are the Sellmeier coefficients that can be obtained by fitting the measured data using the least squares method.

Common prism materials include optical glass, such as BK7, and crystalline materials, such as fused silica (F-Silica), CaF_2, and LiF. At 20 °C and atmospheric pressure, the Sellmeier coefficients and wavelength–refractive index curves of the four materials are presented in Table 2 and Figure 3a, respectively. As shown in Figure 3a, the optical glass materials, such as BK7, are limited in the UV band. As a result, the requirements for a spectral range of 200–300 nm cannot be achieved. The refractive index changes of F-Silica, CaF_2, and LiF at 200–1100 nm are 0.1014, 0.0669, and 0.0503, respectively. It is obvious that the refractive index span of fused silica material is larger in this spectral range.

Table 2. Sellmeier formula constants for common prism materials.

Material	K_1	L_1	K_2	L_2	K_3	L_3
F-Silica	0.6837	0.0046	0.4203	0.0134	0.5850	64.4933
CaF_2	0.5676	0.00253	0.4711	0.01008	3.848	1200.56
LiF	0.9255	0.00544	6.9675	1075.2	0	0
BK7	1.040	0.006	0.2318	0.02002	1.0105	103.56

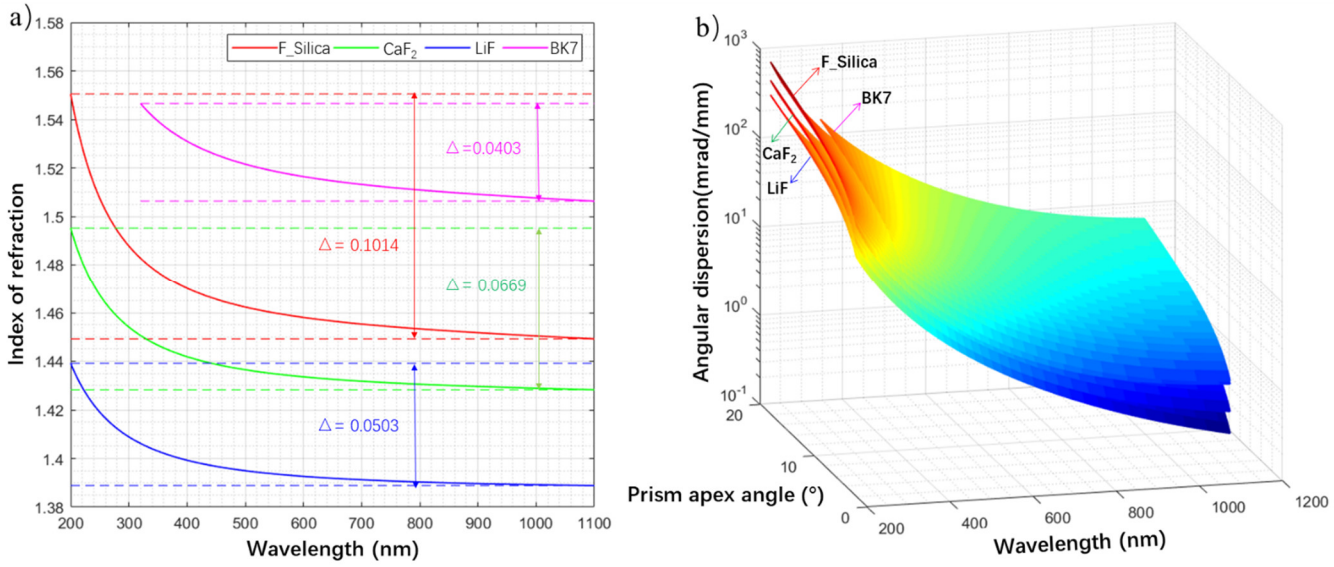


Figure 3. (**a**) Index of refraction versus wavelength. (**b**) Angular dispersion corresponding to different wavelengths and prism apex angles.

According to Equation (8), the angular dispersion of the reflective dispersive prism is [23]:

$$\frac{d\delta}{d\lambda} = \frac{n'(\lambda)\sin\left[2\alpha-\arcsin\left(\frac{\sin i}{n(\lambda)}\right)\right]+\cos\left\{2\alpha-\arcsin\left(\frac{\sin i}{n(\lambda)}\right)\right\}-\frac{n'(\lambda)\sin i}{\sqrt{n^2(\lambda)-\sin i^2}}}{\sqrt{1-n^2(\lambda)\left[2\alpha-\arcsin\left(\frac{\sin i}{n(\lambda)}\right)\right]}}, \quad (9)$$

where i is the incident angle, α denotes the prism apex angle, and $n(\lambda)$ is the refractive index at wavelength λ.

Considering the incident angle of 33° as an example, the angular dispersion of F-Silica, LiF, CaF_2, and BK7 can be estimated based on Equation (9). Figure 3b shows the three-dimensional relationships between the angular dispersion, wavelength, and prism apex angle of these four materials. It is shown that angular dispersion increases with the apex angle of the prism at a constant wavelength for each of the materials. However, as the wavelength increases, the angular dispersion of the prism declines and tends to be uniform for a constant apex angle. This result suggests that the long-wave region features higher requirements for tolerance and image recognition. Comparing the angular dispersion of the four materials, it is worth noting that BK7 shows the highest angular dispersion at a constant wavelength in the spectral range of 320–1100 nm, followed by F-Silica. In fact, F-Silica shows the highest angular dispersion for the full spectral range of 200–1100 nm. Furthermore, given its lower cost and small thermal expansion coefficient, F-Silica is the best choice for auxiliary dispersion components within the spectral range of 200–1100 nm.

3.5. Focusing Lens

The schematic of the single-channel echelle spectrometer is shown in Figure 4.

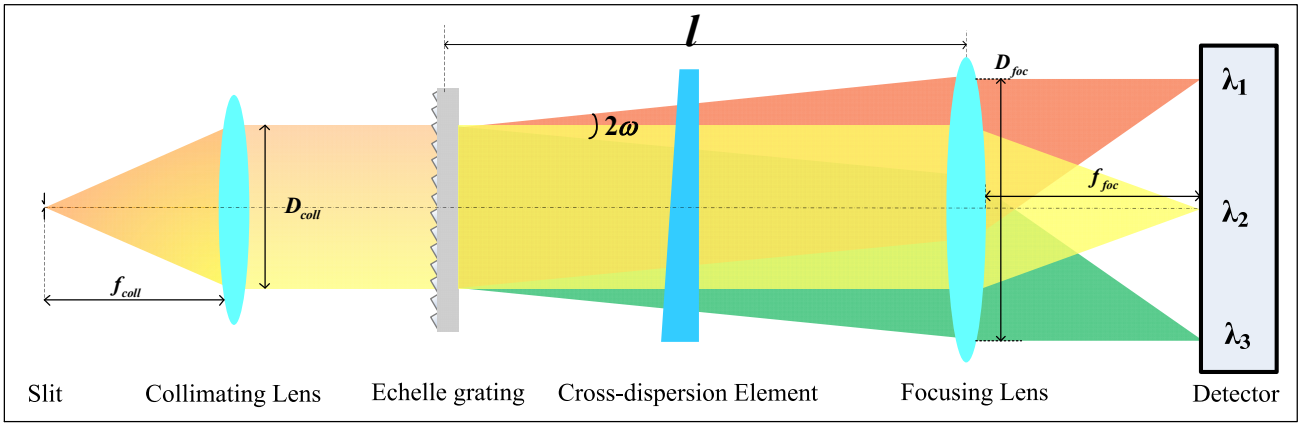


Figure 4. Schematic of the echelle spectrometer.

3.5.1. Determination of Focal Length

The focal length of the focusing mirror is limited by the following factors.

(1) The object–image relationship of the spectrometer: the incident slit of the spectrometer is used as an object. Light of different wavelengths passes through the dispersion system and forms the corresponding images on the same slit at different positions of the detector. The ratio of the size of the slit imaged by the detector to the original size ξ is as follows:

$$\frac{y'}{y} = \frac{y'}{\xi} = \frac{f_{foc}}{f_{coll}}, \tag{10}$$

where y and y' are the height of the object and the image, respectively, and f_{coll} and f_{foc} are the focal lengths of the collimating mirror and focusing mirror, respectively.

(2) Detector pixel size and spectral resolution: according to the Nyquist sampling theorem, the focal length of the focusing lens satisfies the following:

$$f_{foc} \geq \frac{p}{\tan(u'_p)}, \tag{11}$$

where u'_p is the instantaneous field of view of the focusing lens.

Assuming that in critical cases, the number of detector pixels only just satisfies Equation (10), the upper and lower limits of the focal length of the focusing mirror can be calculated as follows.

(1) The upper limit of the focal length of the focusing mirror: the image size of the slit in the detector must be smaller than the size of a single pixel, thus $p \geq y'$; substituted into Equation (10), f_{foc} can be calculated as:

$$f_{foc} \leq \frac{p}{\xi} \times f_{coll}. \tag{12}$$

(2) The lower limit of the focal length of the focusing lens: according to the Nyquist sampling theorem, the wavelength corresponding to the adjacent ±1 pixel of the pixel where the central wavelength is located can be written as follows:

$$\lambda_{center}^{\pm 1} = \lambda_{center} \pm \frac{r}{2}. \tag{13}$$

The diffraction angle $\beta'_{\pm 1}$ corresponding to $\lambda_{center}^{\pm 1}$ satisfies:

$$m\lambda_{center}^{\pm 1} = d \sin\beta_0 \cos\gamma + d \sin\beta'_{\pm 1} \cos\gamma. \tag{14}$$

If we let $\Delta\beta'_{\pm1} = \beta'_{\pm1} - \beta_0$ and substitute it into Equation (11), the focal length is:

$$f_{foc} \geq \frac{p}{\tan(u'_p)} = \frac{p}{\tan(min\{\Delta\beta'_{\pm1}\})}. \quad (15)$$

Combining Equations (12) and (15), the upper and lower limits of the focal length can be expressed as follows:

$$\frac{p}{\tan(min\{\Delta\beta'_{\pm1}\})} \leq f_{foc} \leq \frac{p}{\xi} \times f_{coll}. \quad (16)$$

3.5.2. Determination of Field of View

The angle between the diffracted light at the upper and lower edge wavelengths of the lowest working order of the echelle grating is the maximum field angle of the focusing lens.

The center wavelength $\lambda_{cen\text{-}max}$ corresponding to the lowest order m_{min} is determined by Equation (4) and can be expressed by the following equation:

$$\lambda_{cen-max} = \frac{2d \sin\beta_0 \cos\gamma}{m_{min}}. \quad (17)$$

The diffraction angles corresponding to the upper and lower wavelengths of the free spectral region of this order are:

$$\begin{cases} \beta'_{up} = arc\sin\left(\frac{(m_{min}+1)\lambda_{up}}{d\cos\gamma} - \sin\beta\right) \\ \beta'_{down} = arc\sin\left(\frac{m_{min}\lambda_{down}}{d\cos\gamma} - \sin\beta\right) \end{cases}. \quad (18)$$

Therefore, the field of view of the focusing lens can be estimated as:

$$2\omega = \beta'_{up} - \beta'_{down}. \quad (19)$$

3.5.3. Determination of Aperture Size

For the focusing system, the aperture diaphragm is located in the echelle grating, the size of which is consistent with the effective clear aperture of the collimating lens. Eventually, as shown in Figure 4, the dimensions of the focusing lens can be determined as follows:

$$D_{foc} = D_{coll} + 2l\tan\omega. \quad (20)$$

4. Results and Discussion

All the system parameters mentioned above are shown in Table 3, and the optical structure of the designed spectrometer is shown in Figure 1. The dimensions of the optical system in Figure 1 are approximately 600 mm × 280 mm × 130 mm. The performance in terms of resolution and image quality is analyzed in the following section.

Table 3. Parameters of the echelle gratings.

Parameter		Channel 1	Channel 2	Channel 3
Detection spectrum (nm)		200–500	450–850	800–1100
Groove spacing (lines/mm)		54.5	79	42
Blazing angle (°)		46	63.43	54.74
Diffraction order		52–130	26–50	35–48
Off-axis angle (°)		10	10	10
Focusing lens	Focal Length (mm)	$103 \leq f_{foc1} \leq 170$	$91 \leq f_{foc2} \leq 170$	$116 \leq f_{foc3} \leq 120$
	Field of view (°)	2.3	8.9	4.6
	Aperture size (mm)	34.8	66.1	43.0

4.1. Verification of Spectral Resolution

The grating is used as the main dispersive element with a resolution of $R = mN$, where N is the total number of lines. However, the resolving power is a theoretical limit value, because the slit in the focal plane of the collimator is assumed to be infinitely small and the grating is considered to be an ideal parallel, equal-width, and equally spaced N slit array. In fact, with the incident slit width ξ, the systematic resolution of the grating spectrometer is [24]:

$$\bar{R} = \lambda \frac{f \times m \times N}{\xi \times D \times \cos\theta}, \quad (21)$$

where D and f are the aperture size and focal length of the collimator, respectively.

According to the above parameters for the three channels, the edge and center wavelength resolution capabilities were calculated, and the results are shown in Table 4. Based on the calculation of spectral resolution $\Delta\lambda = \lambda / \overline{R}$, the instrument has a theoretical resolution of better than 0.05 nm over the entire spectral range. The design scheme follows the Nyquist sampling theory and can meet the detection requirements with a resolution of better than 0.1 nm over the full spectral range.

Table 4. Resolution of edge and center wavelengths.

Channel	m	λ(nm)	R	$\overline{R}$	$\Delta\lambda$(nm)
	130	200	180,299	16,319	0.012
Channel 1	74	350	102,632	16,256	0.022
	52	500	72,120	16,319	0.031
	50	450	156,110	31,791	0.014
Channel 2	34	650	106,155	31,226	0.021
	26	850	81,177	31,226	0.027
	48	800	61,734	22,350	0.036
Channel 3	41	950	52,731	22,670	0.042
	35	1100	45,014	22,408	0.049

4.2. Evaluation of Image Quality and Spectral Resolution

The above analysis and calculations show that the completion of calculations for channel 3 are the most difficult. Therefore, if the design can meet the requirements of this channel, then channels 1 and 2 can definitely achieve better resolutions. Therefore, the evaluation of channel 3 is of primary importance.

Figure 5a shows the different order fringes of the spectral signal on the detector of channel 3. In this case, the lowest order, m = 35, corresponds to the longest free spectral region of 31.3 nm. Regardless of the curvature and non-linearity of the fringes, a minimum of 625 pixels is required to achieve a resolution of 0.1 nm. Therefore, the long side of the detector should be almost parallel to the direction of the fringes during assembly. Figure 5b displays the spot diagrams of the upper wavelength of 1100.0 nm ± 0.3 nm with a step size of 0.1 nm. The size of the corresponding image plane of a single square is 20 μm × 20 μm, and the center distance between the adjacent dispersion spots is greater than $2p$ = 30 μm, characteristics that satisfy the Nyquist sampling theorem and can achieve a spectral resolution of 0.1 nm. The spot diagram of the lower wavelength of 800.0 nm ± 0.3 nm with a step size of 0.1 nm is shown in Figure 5c. The size of a single square is 40 μm × 40 μm, so the center distance between the adjacent spots is approximately 40 μm, which is greater than the 30 μm corresponding to 1100.0 nm. This proves that when the focusing mirror is determined, if the spectral interval is fixed at 0.1 nm, the higher the order, the greater the distance between the centers of the adjacent spots. In other words, shorter wavelengths corresponding to higher orders can achieve improved spectral resolution under this condition. Figure 5c,e show that the RMS radii of the spots corresponding to 1100 nm and 800

nm are 0.40 μm and 0.78 μm, respectively, which is considerably smaller than the size of a single pixel, thus ensuring a spectral resolution better than 0.1 nm.

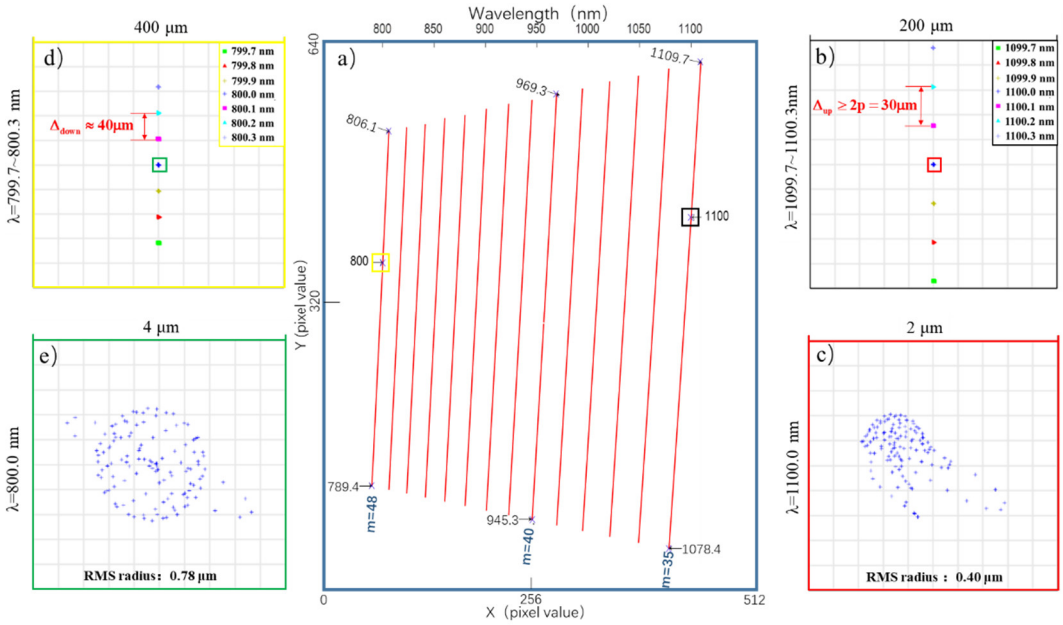


Figure 5. (**a**) Free spectrum of 14 orders on the 640 × 512 detector of channel 3. (**b**,**c**) Spot diagrams of the upper limit wavelength of 1100 nm and its vicinity. (**d**,**e**) Spot diagrams of the lower limit wavelength of 800 nm and its vicinity.

To further verify the rationality of the design, seven equally spaced wavelengths in the free spectral regions corresponding to the highest, lowest, and center orders of channel 3 were selected and simulated. The results are shown in Figure 6, and the size of a single square is 0.5 μm × 0.5 μm. Overall, the spot size of each order shows an increasing trend from the center wavelength to the edge wavelength. The reason is that the center wavelength of each order corresponds to the on-axis field of view of the focusing lens, while the edge wavelength corresponds to the off-axis field of view. In addition, the RMS radius of the spot for all wavelengths is < 1.1 μm, which is considerably smaller than the size of a single pixel, thus proving that the aberrations of the optical system are significantly corrected in the entire spectrum of 800–1100 nm.

Finally, the spectral resolution calculations and image quality evaluation for the full spectral range of 200–1100 nm are displayed in Figures 7–9. The spectral resolutions of all orders of the three channels shown in Figure 7 are better than 0.1 nm, with the highest operating orders of channels 1, 2, and 3 being 130, 50, and 48, respectively, and the corresponding optimal spectral resolutions reaching 0.024 nm at 200 nm, 0.035 nm at 450 nm, and 0.072 nm at 1100 nm, respectively. Based on this, we selected eight wavelengths at equal intervals in the respective spectral ranges of the three channels and traced the rays. Figure 8 shows the spot diagram corresponding to each wavelength. Figure 9 shows the RMS radius curve of the dispersion spot, and the corresponding size of the single square in Figure 8 is 1 μm × 1 μm. It is shown that, over the entire range of the spectrum (200–1100 nm), the maximum RMS radius of the dispersion spot is 2.01 μm and the average RMS radius of the dispersion spot is 0.99 μm, both of which are significantly smaller than the detector pixel radii of 10.625 μm (channels 1 and 2) and 7.5 μm (channel 3). As a result, the aberrations over the entire spectral range can be considered as effectively corrected, which ensures the realization of spectral resolution.

In addition, it is worth noting that the complexity of the system has been increased in order to correct for aberrations, so more attention would need to be paid to the detection of inaccuracies in processing and assembly. The most conventional and convenient

method would be to use a Zygo interferometer to detect any processing inaccuracies in individual components first, and then to measure the aberrations of the combined components to ensure that the image quality of the entire optical system meets expectations.

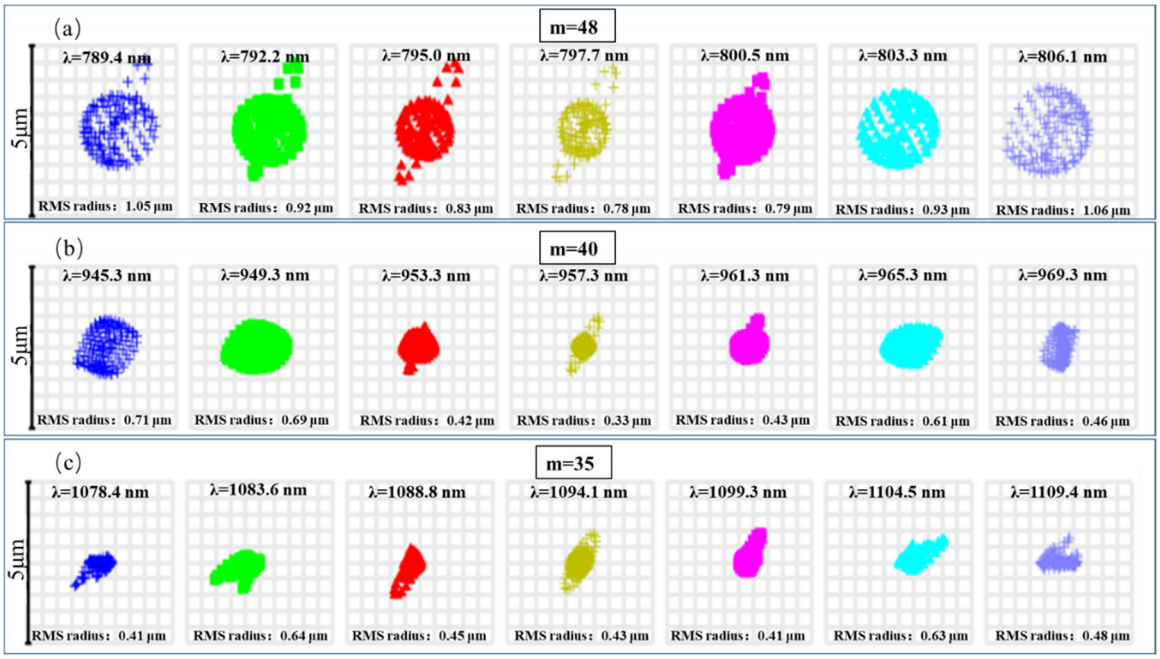


Figure 6. Spot diagrams of seven equally spaced wavelengths: (**a**) m = 48; (**b**) m = 40; (**c**) m = 35.

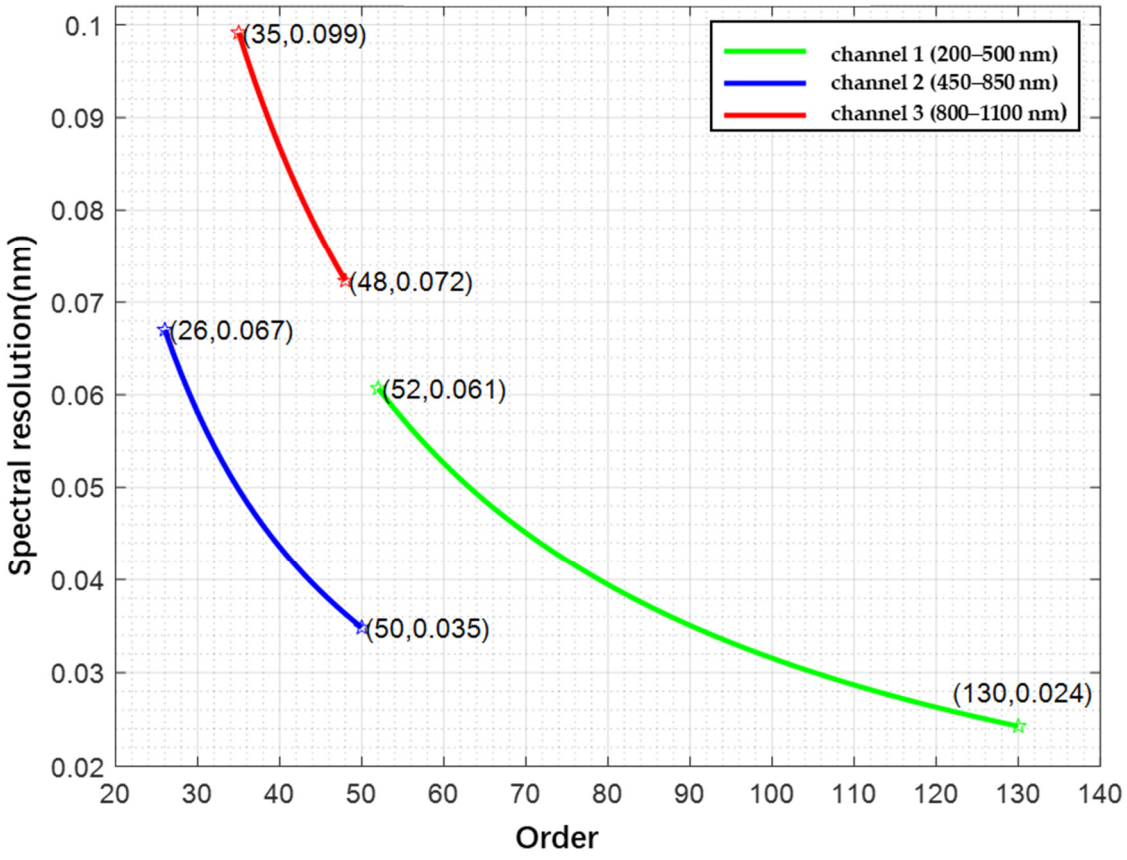


Figure 7. Spectral resolution—order curve of three channels.

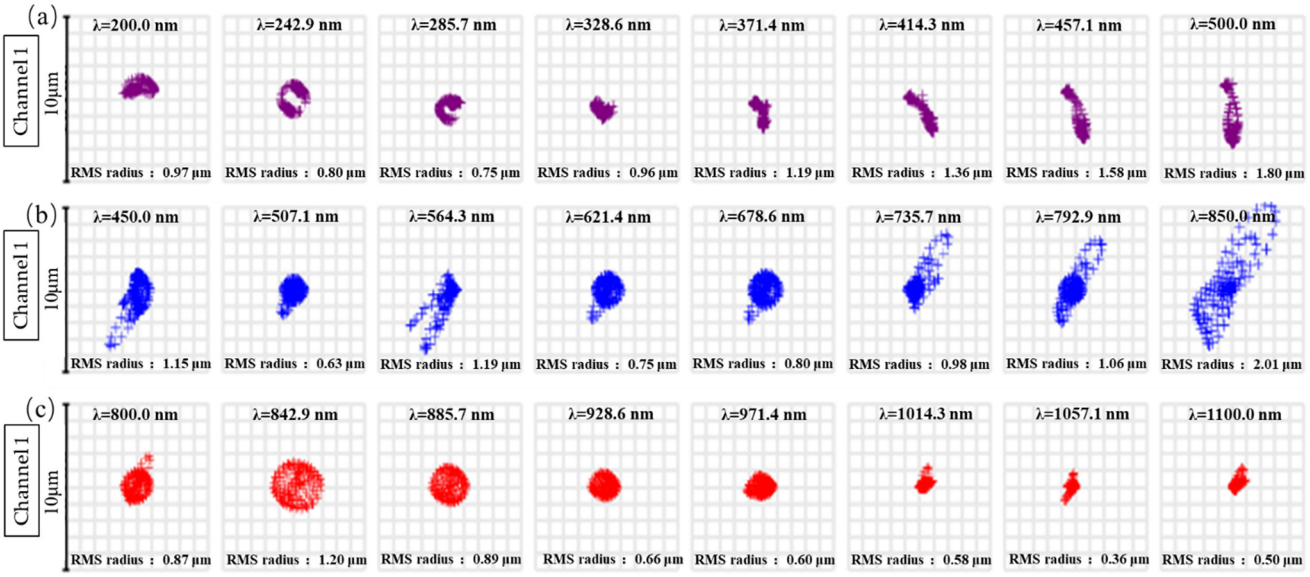


Figure 8. Spot diagrams of eight wavelength points on (**a**) channel 1, (**b**) channel 2, and (**c**) channel 3.

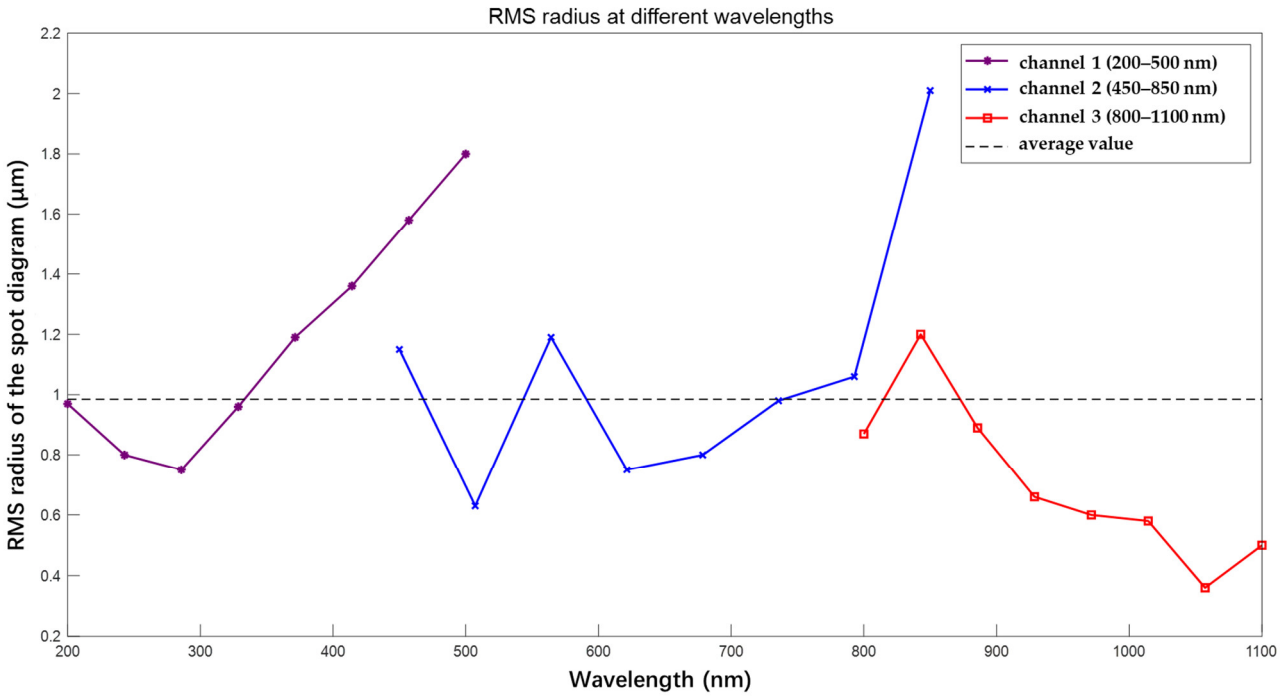


Figure 9. The curve of each spot size in Figure 8.

5. Conclusions

In this paper, a novel optical design of an ultra-wide band spectrometer with a compact asymmetrical C–T structure is proposed. The principle of a high-performance echelle spectrometer design consisting of a slit plane, a parabolic collimator, three echelle gratings, three dispersive prisms, three camera optics, and three detector arrays is presented in detail. The asymmetric design overcomes the limitations of the conventional spectrometer for which the pixels and slits need to be strictly matched. Furthermore, residual aberrations are properly corrected by beneficial increases in the optimization variables. The results reveal that all the spots in the whole spectral range (200–1100 nm) are located within the limited range of the size of the detector. Thus, the spectral resolution of the

echelle spectrometer can reach the theoretical value of 0.024 nm at 200 nm, 0.04 nm at 650 nm), and 0.1 nm at 1100 nm. Overall, the proposed high-performance, real-time, and portable spectrometer is suitable for a wide range of applications.

Author Contributions: Conceptualization, Y.W., Y.Q. and X.F.; methodology, Y.W.; software, Y.W.; validation, Y.W., Y.Q. and X.F.; formal analysis, Y.W. and X.F.; investigation, Y.W. and Y.Q.; resources, Y.W.; data curation, Y.W. and Y.Q.; writing—original draft preparation, Y.W.; writing—review and editing, Y.W.,Y.Q., H.Z. and X.F.; visualization, Y.W.; supervision, X.F. and H.Z.; project administration, Y.Q. All authors have read and agreed to the published version of the manuscript.

Funding: This research received no external funding.

Data Availability Statement: The data presented in this study are available from the corresponding author upon reasonable request.

Acknowledgments: The authors thank Professor Baochang Zhao for his theoretical guidance and academic discussions.

Conflicts of Interest: The authors declare no conflict of interest.

References

1. Henry, M. Spectral Analysis Techniques Using Prism Signal Processing. *Measurement* **2021**, *169*, 108491. https://doi.org/10.1016/j.measurement.2020.108491.
2. Ratheesh, K.M.; Seah, L.K.; Murukeshan, V.M. Spectral Phase-Based Automatic Calibration Scheme for Swept Source-Based Optical Coherence Tomography Systems. *Phys. Med. Biol.* **2016**, *61*, 7652–7663. https://doi.org/10.1088/0031-9155/61/21/7652.
3. Meleppat, R.K.; Matham, M.V.; Seah, L.K. An Efficient Phase Analysis-Based Wavenumber Linearization Scheme for Swept Source Optical Coherence Tomography Systems. *Laser Phys. Lett.* **2015**, *12*, 055601. https://doi.org/10.1088/1612-2011/12/5/055601.
4. Harrison, G.R. The Production of Diffraction Gratings: II The Design of Echelle Gratings and Spectrographs1. *J. Opt. Soc. Am.* **1949**, *39*, 522. https://doi.org/10.1364/JOSA.39.000522.
5. Muhammed Shameem, K.M.; Dhanada, V.S.; George, S.D.; Kartha, V.B.; Santhosh, C.; Unnikrishnan, V.K. Assessing the Feasibility of a Low-Throughput Gated Echelle Spectrograph for Laser-Induced Breakdown Spectroscopy (LIBS)-Raman Measurements at Standoff Distances. *Opt. Laser Technol.* **2022**, *153*, 108264. https://doi.org/10.1016/j.optlastec.2022.108264.
6. Gibbs, A. Limits on the Auroral Generation of H_3^+ in Brown Dwarf and Extrasolar Giant Planet Atmospheres with the Keck Near Infrared Echelle Spectrograph. *Astron. J.* **2022**, *164*, 63.
7. Weber, M.; Woche, M.; Ilyin, I.; Strassmeier, K.G.; Oliva, E. ANDES, the High Resolution Spectrometer for the ELT: The UBV Spectrograph Module. In Proceedings of the Ground-based and Airborne Instrumentation for Astronomy IX, Montréal, QC, Canada, 29 August 2022; Volume 12184, pp. 1070–1076.
8. Jakobsen, P.; Ferruit, P.; Alves de Oliveira, C.; Arribas, S.; Bagnasco, G.; Barho, R.; Beck, T.L.; Birkmann, S.; Böker, T.; Bunker, A.J.; et al. The Near-Infrared Spectrograph (NIRSpec) on the James Webb Space Telescope: I. Overview of the Instrument and Its Capabilities. *Astron. Astrophys.* **2022**, *661*, A80. https://doi.org/10.1051/0004-6361/202142663.
9. Itoh, S.; Ishihara, D.; Wada, T.; Nakagawa, T.; Oyabu, S.; Kaneda, H.; Hirahara, Y. Simulations of the Spectral Resolving Power of a Compact Space-Borne Immersion-Echelle Spectrometer Using Mid-Infrared Wave Tracing. *J. Astron. Telesc. Instrum. Syst.* **2022**, *8*, 025004. https://doi.org/10.1117/1.JATIS.8.2.025004.
10. Feng, L.; He, X.; Li, Y.; Wei, L.; Nie, Y.; Jing, J.; Zhou, J. Compact Shortwave Infrared Imaging Spectrometer Based on a Catadioptric Prism. *Sensors* **2022**, *22*, 4611. https://doi.org/10.3390/s22124611.
11. Shafer, A.B.; Megill, L.R.; Droppleman, L. Optimization of the Czerny–Turner Spectrometer. *J. Opt. Soc. Am.* **1964**, *54*, 879. https://doi.org/10.1364/JOSA.54.000879.
12. Green, J.C. Aberration Corrected Designs for High Resolution Echelle Spectroscopy in the Far Ultraviolet. In Proceedings of the Space Telescopes and Instrumentation 2022: Ultraviolet to Gamma Ray, Montréal, Canada, 31 August 2022; den Herder, J.-W.A., Nakazawa, K., Nikzad, S., Eds.; SPIE: Montréal, Canada, 2022; p. 101.
13. Gil, M.A.; Simon, J.M.; Fantino, A.N. Czerny-Turner Spectrograph with a Wide Spectral Range. *Appl. Opt.* **1988**, *27*, 4069. https://doi.org/10.1364/AO.27.004069.
14. Xue, Q.; Wang, S.; Lu, F. Aberration-Corrected Czerny-Turner Imaging Spectrometer with a Wide Spectral Region. *Appl. Opt.* **2009**, *48*, 11. https://doi.org/10.1364/AO.48.000011.
15. Zheng, L.; Susa, A.J.; Hanson, R.K. Methodology of Designing Compact Schlieren Systems Using Off-Axis Parabolic Mirrors. *Appl. Opt.* **2022**, *61*, 4857. https://doi.org/10.1364/AO.457151.
16. Allemand, C.D. Coma Correction in Czerny–Turner Spectrographs. *J. Opt. Soc. Am.* **1968**, *58*, 159. https://doi.org/10.1364/JOSA.58.000159.
17. Foreman, W.T. Lens Correction of Astigmatism in a Czerny-Turner Spectrograph. *Appl. Opt.* **1968**, *7*, 1053. https://doi.org/10.1364/AO.7.001053.

18. Li, S.; Zhao, W.; Xu, H.; Qiu, L.; Wang, Y. Optical System Design of Aberration-Corrected Czerny–Turner Imaging Spectrometer with High Resolution. *Opt. Commun.* **2020**, *459*, 125015.
19. Dong, J.; Chen, H.; Zhang, Y.; Chen, S.; Guo, P. Miniature Anastigmatic Spectrometer Design with a Concave Toroidal Mirror. *Appl. Opt.* **2016**, *55*, 1537. https://doi.org/10.1364/AO.55.001537.
20. Dalton, M.L. Astigmatism Compensation in the Czerny–Turner Spectrometer. *Appl. Opt.* **1966**, *5*, 1121. https://doi.org/10.1364/AO.5.001121.
21. Fu, X. Optical Design of a Broadband Spectrometer with Compact Structure Based on Echelle and Concave Gratings. *Opt. Lasers Eng.* **2022**, *151*, 106926.
22. Yuan, B.; Guo, Y.; Liu, Z. The Influence of Light Path Length on the Color of Synthetic Ruby. *Sci. Rep.* **2022**, *12*, 5943. https://doi.org/10.1038/s41598-022-08811-y.
23. Xue, Q.; Yang, B.; Tian, Z.; Luan, X.; Mu, B.; Wang, S. Spaceborne Limb Hyperspectral Imager for Ozone Profile Detection. *Opt. Express* **2019**, *27*, 31348–31361.
24. Bingham, R.G. Grating Spectrometers and Spectrographs Re-Examined. *Q. J. R. Astron. Soc.* **1979**, *20*, 395–421.